

See discussions, stats, and author profiles for this publication at: <https://www.researchgate.net/publication/228326995>

Electrospun TiO₂–Graphene Composite Nanofibers as a Highly Durable Insertion Anode for Lithium Ion Batteries

ARTICLE in THE JOURNAL OF PHYSICAL CHEMISTRY C · JUNE 2012

Impact Factor: 4.77 · DOI: 10.1021/jp302574g

CITATIONS

80

READS

234

6 AUTHORS, INCLUDING:



Palaniswamy Suresh Kumar

Center of Innovation, Singapore

58 PUBLICATIONS 1,056 CITATIONS

SEE PROFILE



Vanchiappan Aravindan

Nanyang Technological University

145 PUBLICATIONS 2,725 CITATIONS

SEE PROFILE



Sundaramurthy Jayaraman

Ngee Ann Polytechnic

67 PUBLICATIONS 929 CITATIONS

SEE PROFILE

Electrospun TiO₂–Graphene Composite Nanofibers as a Highly Durable Insertion Anode for Lithium Ion Batteries

Xiang Zhang,^{†,||,#} Palaniswamy Suresh Kumar,^{||,#,§} Vanchiappan Aravindan,^{†,§} Hui Hui Liu,^{‡,#} Jayaraman Sundaramurthy,^{||,§} Subodh G. Mhaisalkar,[†] Hai Minh Duong,[†] Seeram Ramakrishna,^{*,†,§} and Srinivasan Madhavi^{*,||,†}

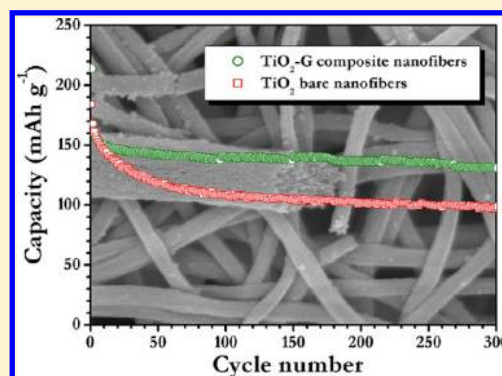
[†]Department of Mechanical Engineering, [‡]Department of Chemistry, and [§]Center for Nanofibers and Nanotechnology, National University of Singapore, Singapore 117576, Singapore

^{||}School of Materials Science and Engineering, Nanyang Technological University, Singapore 639798, Singapore

[†]Energy Research Institute @ NTU (ERI@N), Nanyang Technological University, Research Techno Plaza, 50 Nanyang Drive, Singapore 637553, Singapore

S Supporting Information

ABSTRACT: We report the synthesis and electrochemical performance of one-dimensional TiO₂–graphene composite nanofibers (TiO₂–G nanofibers) by a simple electrospinning technique for the first time. Structural and morphological properties were characterized by various techniques, such as X-ray diffraction, scanning electron microscopy (SEM), transmission electron microscopy (TEM), Raman spectroscopy, and BET surface area analysis. Lithium insertion properties were evaluated by both galvanostatic and potentiostatic modes in half-cell configurations. Cyclic voltammetric study reveals the Li-insertion/extraction by a two-phase reaction mechanism that is supported by galvanostatic charge–discharge profiles. Li/TiO₂–G half-cells showed an initial discharge capacity of 260 mA h g^{−1} at current density of 33 mA g^{−1}. Further, Li/TiO₂–G cell retained 84% of reversible capacity after 300 cycles at a current density of 150 mA g^{−1}, which is 25% higher than bare TiO₂ nanofibers under the same test conditions. The cell also exhibits promising high rate behavior with a discharge capacity of 71 mA h g^{−1} at a current density of 1.8 A g^{−1}.



1. INTRODUCTION

Lithium ion battery (LIB) technology has been the forerunner in portable and mobile applications. Their performance, however, still lags behind for emerging applications such as electric vehicles (EV) and hybrid electric vehicles (HEV).^{1–3} New LIB electrode materials that would offer not only high specific capacities but also safety and cycling durability are essential for high-volume LIB applications.^{4,5} Titanium dioxide, TiO₂ (anatase), has emerged as a promising LIB anode alternative due to its high theoretical capacity (335 mA h g^{−1}), flat operating potential (arising from two phase-reaction mechanism), and low volume expansion during lithium intercalation/deintercalation (3–4%) leading to long cycle life and durability. In addition, TiO₂ is an abundant, low-cost, environmentally benign electrode material that offers enhanced safety as compared to graphite, owing to its higher insertion potential (~1.7 V vs Li) that prohibits lithium plating.^{6,7}

However, the practical electrochemical performance of anatase-TiO₂ is still not optimal due to poor electron transport, aggregation tendency of TiO₂ nanoparticles, slow Li ion diffusion, and inherent electronic conductivity issues. Ongoing research activities are targeted toward improving the ionic and electronic transport properties of titania. One such approach is

tailoring particle size and morphology of anatase TiO₂ to enhance lithium diffusion and electronic conduction path. One-dimensional (1D) metal oxide nanostructured materials such as nanowires, nanotubes, and nanorods are particularly interesting in LIBs owing to the large surface to volume ratio, their vectorial ion and electron transport, and ability to accommodate lithiation induced stresses.^{8–11} To date, considerable efforts have been devoted to the synthesis of TiO₂ nanomaterials with various morphologies through different routes such as sol–gel, micelle, reverse micelle, and hydrothermal/solvothermal methods.^{8,9,12} Another approach to improve the Li ion insertion properties of titania is to fabricate composite nanostructured electrodes that interconnect titania with a conducting additive nanophase (such as carbon, CNT) that provides a facile electron pathway.^{13,14}

Similarly, graphene-based materials have also been emerged as prospective electrodes in LIB applications because of their unique properties like high specific surface area (2630 m² g^{−1}), high intrinsic mobility (200 000 cm² v^{−1} s^{−1}), high Young's

Received: March 16, 2012

Revised: June 19, 2012

Published: June 28, 2012

modulus (1.0 TPa), thermal conductivity ($5000 \text{ W m}^{-1} \text{ K}^{-1}$), optical transmittance ($\sim 97.7\%$), and excellent electrical conductivity.^{15–17} Graphene has been considered as anode material for LIBs with the theoretical capacity of 744 mA h g^{-1} based on the turbostatic lithium storage mechanism (Li_2C_6). Owing to its superior electrical conductivity and mechanical stability, several hybrid nanocomposites consisting of graphene and electroactive material (viz. Co_3O_4 , Fe_2O_3 , SnO_2 , MnO_2 , $\text{Li}_4\text{Ti}_5\text{O}_{12}$, etc.) have also been synthesized and tested in LIB.^{18–24}

In the present study, we have fabricated electrospun TiO_2 –graphene (TiO_2 –G) one-dimensional nanofibers to improve the electrical conductivity and Li ion diffusion pathways of anatase TiO_2 .²⁵ A scalable, low-cost electrospinning technique was employed to synthesize one-dimensional anatase- TiO_2 nanofibers that would enhance the Li diffusion properties.^{26,27} The electrospinning technique has been well-demonstrated to pattern the materials in one-dimensional structures for various applications such as Li ion batteries,^{28,29} dye-sensitized solar cells (DSSC),^{30,31} photocatalysis,^{31,27} etc. Lithium insertion properties of TiO_2 –G nanofibers were evaluated in half-cell configurations and compared with bare TiO_2 electrospun nanofibers. Promising high rate lithium intercalation behavior was exhibited by TiO_2 –graphene nanofibers as compared to the pristine ones, demonstrating their potential as a prospective anode for high-performance LIB applications.

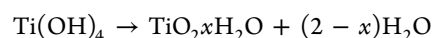
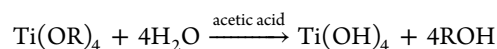
2. EXPERIMENTAL SECTION

2.1. Materials. Polystyrene (PS, $M_n = 192\,000$), titanium isopropoxide (TIP, 97%), *N,N*-dimethylformamide (DMF, 99.8%), and acetic acid (99.7%) were purchased from Sigma-Aldrich and used as received.

2.2. Synthesis of Graphene. Graphene nanosheets were synthesized by chemical reduction of exfoliated graphene oxide using a modified Hummers method. First, 2 g of NaNO_3 was dissolved in 100 mL of concentrated H_2SO_4 in an ice bath. Four grams of commercial graphite powder (Sigma Aldrich) and 14.6 g of KMnO_4 were slowly added into this mixture, and the temperature was maintained below 20°C with vigorous stirring for 2 h. The temperature of this mixture was increased to 35°C and the mixture was stirred at this temperature for 12 h to form a brown paste. Deionized water (DI water) (180 mL) was added to the mixture, it was stirred for 15 min, and 110 mL of DI water and 14 mL of 30% H_2O_2 were consequently added into the mixture to compete the oxidation process. The color of the mixture changed from brown to yellow. The mixture was washed with 1 M HCl and DI water to remove residual ions and dried at 60°C under ambient conditions. Exfoliation was carried out by sonicating the graphene oxide (500 mg) in deionized water (500 mL) for 1 h followed by reduction with NaBH_4 (1.5 g) for 24 h and centrifugation for 10 min to separate the graphene nanosheets. The solution pH was adjusted in the range of 9–10 using Na_2CO_3 or NaOH. The as prepared graphene was centrifuged and washed with deionized water and dried at 60°C (see Supporting Information).

2.3. Preparation of Graphene–Titanium Dioxide Composite Nanofibers. Graphene (40 mg) and 10 mL of DMF were sonicated for 12 h to disperse graphene nanosheets into DMF solution. PS (1.5 g) was then added to the above solution, the mixture was stirred for 24 h, and 3 mL of acetic acid and 1.5 g of TIP were slowly added into the above mixture and it was stirred continuously for 12 h to yield homogeneous

solution. The prepared homogeneous solution was loaded into plastic syringes (10 mL) and subsequently placed into a commercial electrospinning setup (NANON, MECC Japan). A high-voltage power of 25 kV was applied to the needle tip. The flow rate of fluid was set to 1 mL/h. The humidity level inside the electrospinning chamber was $55 \pm 5\%$. The nanofibers were collected on aluminum foil wrapped around a flat plate placed 12 cm below the needle tip (22 G). The electrospun TiO_2 –graphene composite nanofibers were then calcined at 450°C for 1 h in Ar environment to decompose polystyrene.³² The heating and cooling rate was set to be $5^\circ\text{C}/\text{min}$. During the electrospinning process, the liquid droplet containing the TIP, polymer, and ethanol becomes charged when a sufficiently high voltage is applied and electrostatic repulsion counteracts the surface tension and the droplet is stretched. The fine nanofibers were then drawn using the electrical charge. During the formation of the nanofibers, the solvent was evaporated away and the polystyrene was solidified into nanofibers instantly, followed readily by the hydrolyzation of TIP catalyzed by acetic acid and condensation of titanium alkoxides to form TiO_2 . The process is schematically represented below and transformation of the anatase phase usually occurred after 400°C .³³



R = isopropyl

2.4. Characterizations and Electrochemical Measurements. Powder X-ray diffraction measurement was carried out using Bruker AXS D8 Advance X-ray diffractometer equipped with $\text{Cu K}\alpha$ radiation between 10° and 80° . The morphological features and chemical composition were examined with a field emission scanning electron microscope (FE-SEM, JEOL-6701F) with an energy dispersive X-ray spectrometer (EDS) attachment. Particle morphology of the synthesized composites was observed using transmission electron microscopy (TEM, JEOL 3010) and selected area electron diffraction (SAED). Specimens were prepared by ultrasonically dispersing TiO_2 –graphene composite nanofibers in ethanol followed by dropping the suspension on a carbon-coated copper grid. The surface area and pore volume were determined by nitrogen adsorption/desorption using the Brunauer–Emmett–Teller method (BET, Micromeritics Tristar 2000, surface area and pore size analyzer). The sample was degassed under inert nitrogen (N_2) at 300°C for 12 h prior to BET measurements (under standard protocols at 77 K). All the electrochemical studies were conducted in two-electrode coin-cell (CR 2016) configuration. In the electrochemical measurements, metallic lithium was used both as counter and reference electrodes. The composite anode was formulated with 10 mg of active material (TiO_2 –G nanofibers), 1 mg of super P, and 2 mg of binder (Teflonized acetylene black, TAB-2). This mixture was pressed on a 200 mm^2 stainless steel mesh, which serves as current collector, and subsequently dried at 60°C overnight before conducting cell assembly in an Ar-filled glovebox (MBraun). The electrodes were separated by a microporous glass fiber separator (Whatman, Cat. No. 1825-047). Standard 1 M LiPF_6 in ethylene carbonate (EC)/diethyl carbonate (DEC) (1:1 wt %, DAN VEC) mixture was used as the electrolyte solution. Cyclic voltammetric (CV) traces were recorded using a Solartron 1470E and SI 1255B impedance/gain-phase analyzer coupled with a potentiostat in two-electrode configuration.

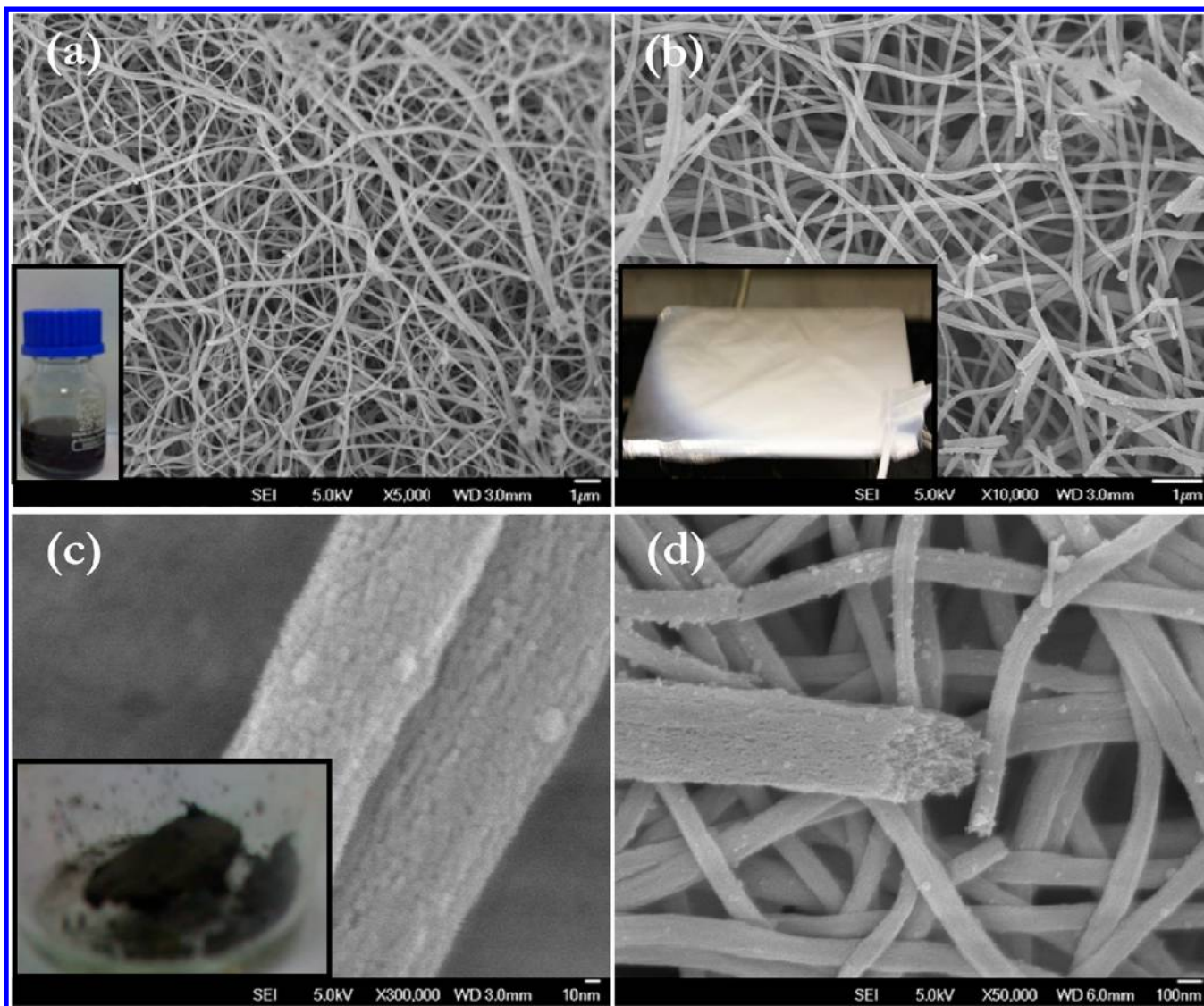


Figure 1. (a) FE-SEM image of a bundle of as-spun TiO_2 –graphene composite nanofiber mats. Inset is the optical image of as-prepared sol–gel solution before electrospinning. (b) FE-SEM image of a bundle of TiO_2 –graphene composite nanofiber mats sintered at 450°C in Ar atmosphere. Inset is the optical image of as-electrospun TiO_2 –graphene composite nanofibers before heat treatment. (c) Magnified FE-SEM image of the surface of TiO_2 –graphene composite nanofibers. Inset is the optical image of as-electrospun TiO_2 –graphene composite nanofibers after heat treatment. (d) FE-SEM image of the tip of TiO_2 –graphene composite nanofibers at a different magnification.

Galvanostatic cycling profiles were recorded using an Arbin 2000 battery tester at various current densities between 1 and 3 V at room temperature.

3. RESULTS AND DISCUSSION

Field emission scanning electron microscopy (FE-SEM) was performed to investigate the morphological features of TiO_2 –G nanofibers. Figure 1a presents an FE-SEM micrograph of as-spun TiO_2 –G composite nanofibers. The image clearly indicates the formation of highly interconnected networks of fibers. In order to ensure the formation of homogeneous solution before spinning, an optical image has been recorded and is presented as an inset of Figure 1a. The optical image of as-prepared sol–gel is dark black due to the presence of graphene nanosheets in the solution. Figure 1b shows a FE-SEM image of TiO_2 –graphene composite nanofibers after the calcination at 450°C for 1 h under Ar atmosphere. The inset picture represents the optical image of as-spun TiO_2 –graphene

composite nanofibers showing the color of the fibers to be pure white. The image clearly reveals the retention of fibrous morphology after the heat treatment. High magnification FESEM micrographs of TiO_2 –G nanofibers reveal that a highly porous surface of fibers is evidently seen from the higher magnification of the TiO_2 –G nanofibers pictures (Figure 1c,d). The inset in Figure 1c shows the optical image of sintered fibers that appeared black in color. An electrospun fiber diameter of 100–200 nm is obtained after heat treatment, as seen from FESEM images (Figure 1c,d). An energy dispersive X-ray spectrum (EDS) of TiO_2 –G nanofibers also recorded along with elemental mapping is presented Figure 2. The EDS analysis revealed the molar ratio of Ti and O to be 1:2 for the above fibers, which is in good agreement with the stoichiometric ratio of TiO_2 . Carbon content (graphene) estimated from EDS analysis was found to be 9.9 wt %. TGA analysis of PS under Ar atmosphere clearly indicates the negligible amount of pyrolyzed carbon (0.47 wt %) present in

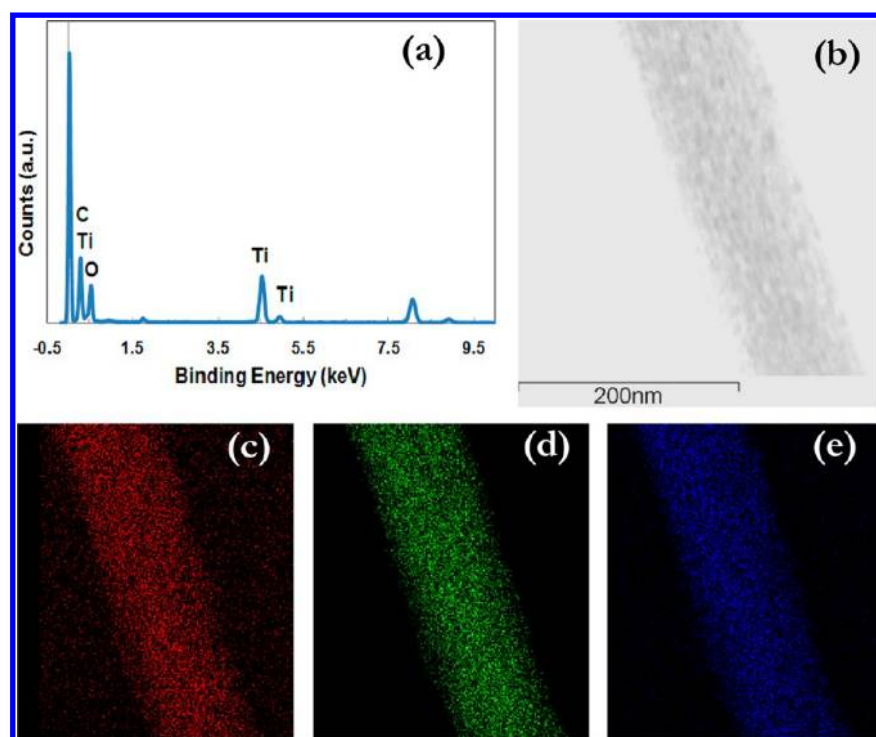


Figure 2. (a) EDS spectrum of TiO_2 –graphene composite nanofibers. (b) Corresponding TEM image of a single TiO_2 –graphene composite nanofiber for elemental mapping. Mapping of (c) carbon, (d) titanium, and (e) oxygen.

the TiO_2 –G nanofibers during decomposition (Figure S3, Supporting Information). The results of TEM examination combined with the corresponding EDS mapping for the elements of C, Ti, and O are presented in Figure 2b–e. No other impurity phases were seen in the samples. The mapped red, green, and blue regions correspond to carbon, titanium, and oxygen elements, respectively, indicating a homogeneous distribution of graphene and TiO_2 throughout the electrospun nanofiber. One dimensional nanofiber morphology coupled with a uniform distribution of conducting graphene nanosheets would certainly provide faster electronic transport and lithium diffusion in TiO_2 –G nanofibers during electrochemical lithium intercalation/deintercalation.

The microstructure of TiO_2 –graphene composite nanofibers was further examined by transmission electron microscopy (TEM) and is presented in Figure 3. Figure 3a shows the typical microstructure of a single TiO_2 –G nanofiber with voids. The highly crystalline TiO_2 was uniformly distributed in the graphene nanosheets in a broad area to form the composite materials. The corresponding crystalline diffraction rings of (101), (004), (200), and (105) in the selected area electron diffraction (SAED) patterns (Figure 3b) confirmed the formation of polycrystalline TiO_2 anatase phase in TiO_2 –graphene composite nanofiber. As shown in Figure 3c,d, the high-resolution TEM image revealed that the TiO_2 –G nanofibers possessed a well-crystallized structure, and lattice fringes of TiO_2 comprise an interplanar spacing of 0.35 nm, corresponding to the (101) plane of anatase phase. There is unambiguous evidence that the TiO_2 crystals were sandwiched between a few layers of graphene nanosheets with a particular lattice spacing of 0.35 nm.

The powder X-ray diffraction (XRD) pattern of TiO_2 –G nanofibers sintered at 450 °C is given in Figure 4a. The XRD reflections showed the presence of phase-pure anatase TiO_2

structure in nanofibers that belongs to the body-centered type with space group $I4_1/amd$. No impurity phases were seen. The anatase TiO_2 structure consists of TiO_6 octahedra sharing two adjacent edges with two other octahedral sites, so that planar double chains are formed. In this case, Li ion diffusion takes places along a reaction path connecting the octahedral interstitial sites. Rietveld refinement was conducted using TOPAS V3 software for the observed X-ray reflections to calculate the lattice parameters and found to be $a = 3.793(9)$ Å and $c = 9.482(5)$ Å. The observed values are consistent with the literature (JCPDS 89-4203). Crystallite size was calculated using Scherrer formulas and found to be 6 nm. Figure 4b shows the Raman spectrum of TiO_2 –graphene composite nanofibers recorded between 200 and 1800 cm^{-1} . Raman spectra showed the broadened characteristic frequencies at ~ 1351 and ~ 1600 cm^{-1} , which correspond to the D and G bands, respectively.³⁴ Frequencies at ~ 398 and 499 cm^{-1} are assigned to the B_{1g} and A_{1g} vibrational modes of TiO_2 anatase phase, respectively.^{35,36} The intensity ratio of D and G bands (I_D/I_G) provides useful information about the degree of crystallinity of the graphene nanosheets. Higher intensity ratio means the higher defect concentration in the graphite comprising sp^2 hybridization. The intensity ratio I_D/I_G in TiO_2 –G was found to be 0.76, indicating a lower crystallinity degree that can be ascribed to the presence of graphene layers, which increases the concentration of defects in graphite structure.³⁷

Figure 5a shows the N_2 adsorption–desorption isotherms of the TiO_2 –G and bare TiO_2 nanofibers. The corresponding texture properties of TiO_2 –G and bare TiO_2 nanofibers are summarized in Table 1. The TiO_2 –G nanofibers exhibits type IV isotherm curves with a well-defined characteristic condensation step at $P/P_0 = 0.3$ – 0.5 that clearly indicates the mesoporous nature of TiO_2 –graphene composite nanofibers. The intersection point in the N_2 adsorption/desorption curves

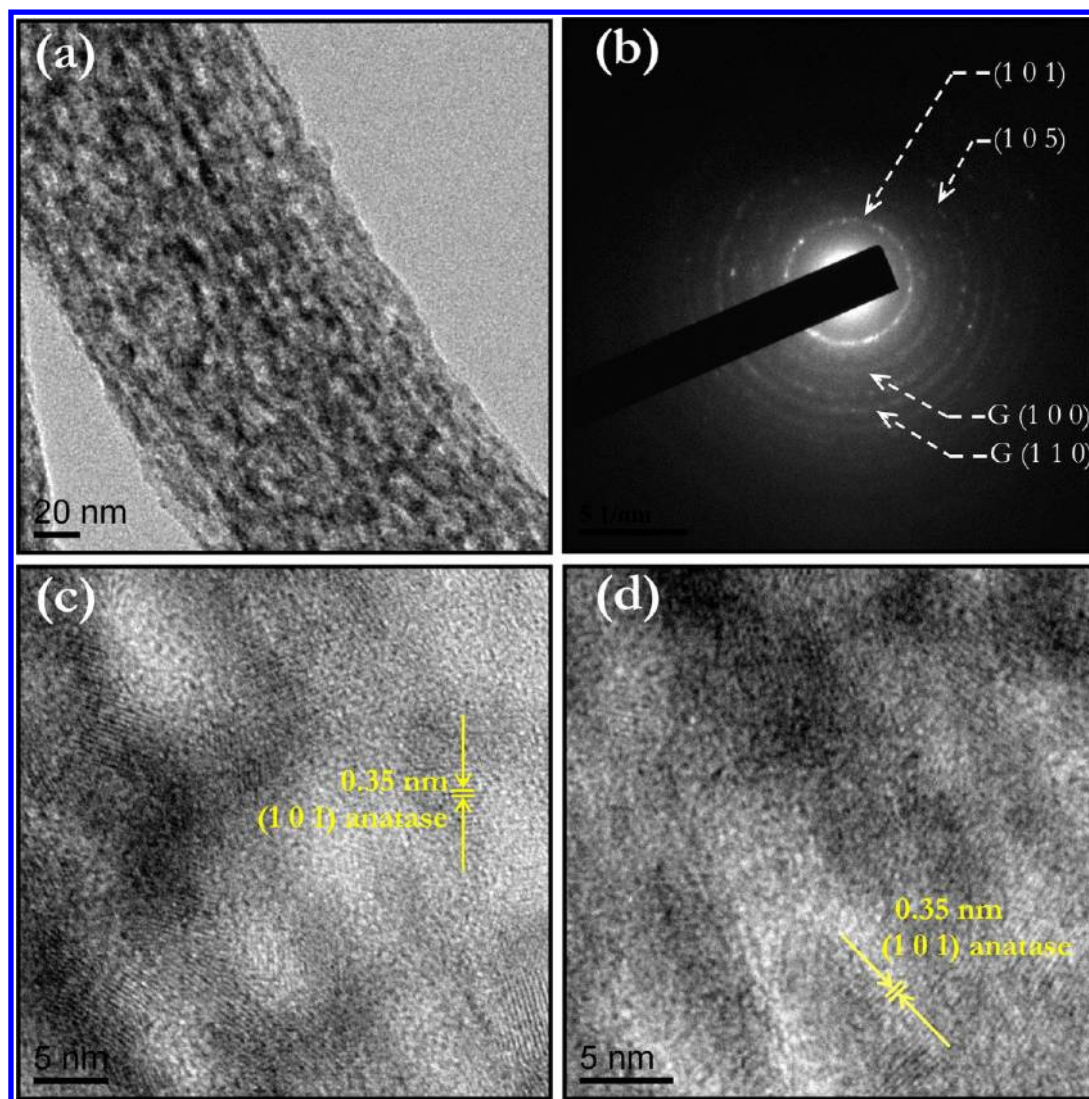


Figure 3. (a) TEM image of a single TiO_2 –graphene composite nanofibers. (b) Corresponding SAED pattern, in which G corresponds to graphene and rest of the hkl planes belongs to anatase TiO_2 phase. (c and d) HR-TEM images of TiO_2 –graphene composite nanofibers. (The anatase TiO_2 phase is indicated by the yellow line.)

of TiO_2 –G nanofibers demonstrated that the surface contained uniformly sized pores. The pore size distribution was calculated on the basis of the Barrett–Joyner–Halenda (BJH) method. A narrow pore size with average pore diameter of 10.6 and 18.2 nm was observed for TiO_2 –G nanofibers and bare TiO_2 nanofibers, respectively. BET study revealed that the TiO_2 –G nanofibers had a specific surface area of $191 \pm 5 \text{ m}^2 \text{ g}^{-1}$, which is about 3 times higher than that of bare TiO_2 nanofibers ($52 \pm 4 \text{ m}^2 \text{ g}^{-1}$). The total pore volume of TiO_2 –G nanofibers and bare TiO_2 nanofibers were found to be 0.4 and $0.239 \text{ cm}^3 \text{ g}^{-1}$, respectively. The higher specific surface area is one of the prerequisites for the electrode materials, since highly exposed surface area facilitates faster diffusion of Li ions due to the extended electrode/electrolyte interface.

Electrochemical performances of bare and TiO_2 –G nanofibers were evaluated in half-cell configuration (Li/ TiO_2 or TiO_2 –G) between 1 and 3 V in room temperature. Half-cells were subjected to cyclic voltammetric (CV) measurements at scan rate of 0.1 mV s^{-1} , in which metallic lithium acts as counter and reference electrode, respectively. The CV traces of Li/ TiO_2 –G cells for the first three cycles are presented in

Figure 6a. The cell showed an open circuit voltage (OCV) of $\sim 2.90 \text{ V}$ vs Li. The cell was first discharged to enable insertion of lithium ions in to TiO_2 crystal lattice, resulting in a change in valence state of titanium from Ti^{4+} to Ti^{3+} . The CV traces showed sharp peaks at ~ 1.66 and $\sim 2.07 \text{ V}$ during cathodic and anodic sweeps, respectively. The cathodic scan corresponds to the Li insertion and the anode sweep indicates extraction of the Li ions. Reduction of Ti^{4+} into Ti^{3+} during the cathodic scan and subsequent oxidation to 4+ during anodic scan indicates the excellent reversibility of the anatase- TiO_2 –graphene insertion host. The sharp oxidation/reduction peaks reveal the two-phase reaction mechanism during electrochemical lithium insertion/extraction according to the following equilibrium: $\text{TiO}_2 + x\text{Li}^+ + xe^- \leftrightarrow \text{Li}_x\text{TiO}_2$.³⁸ However, in the subsequent cycles, small deviations in the peak positions are noted, possibly due to structural rearrangement of TiO_2 crystal lattice. The bare TiO_2 nanofibers also exhibited a similar kind of redox reaction, except variation in the intensity of the peaks and a slight shift in the potential toward higher voltage are noted. The sharp, intense peaks clearly show the extended two-phase

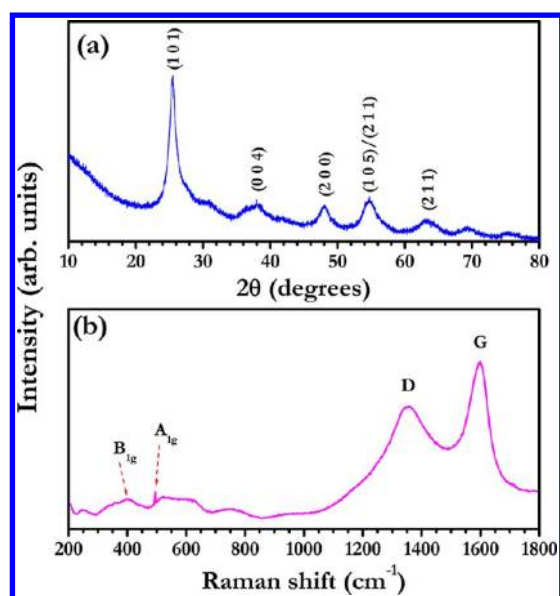


Figure 4. (a) Powder X-ray diffraction patterns of TiO₂-graphene composite nanofibers and (b) Raman spectrum of TiO₂-graphene composite nanofibers.

reaction when compared to the bare TiO₂ nanofibers (Figure 6b).

Galvanostatic cycling profiles of Li/TiO₂-G half-cells are performed between 1 and 3 V at a constant current density of 33 mA g⁻¹ in room temperature. The typical signature of the charge-discharge curves for first two cycles of Li/TiO₂-G cells are given in Figure 7a. First, the cell has been discharged to intercalate lithium ions into the TiO₂ matrix. During Li insertion, TiO₂ lattice undergoes a first-order phase transition from tetragonal (*I*₄/amd) to orthorhombic (Li_{0.5}TiO₂, space group *Pnm*2₁) phase, which is due to the loss of symmetry in the *y* direction. This phase transition occurs along with a spontaneous phase separation of lithium-poor (Li_{0.01}TiO₂) into lithium-rich (Li_{0.5}TiO₂) phase that has been previously reported by several researchers.^{6,39} The cell delivered the

Table 1. Texture of Properties TiO₂-Graphene Composite Nanofibers and Bare TiO₂ Nanofibers

morphology	BET surface area (m ² /g)	av pore diameter (nm)	total pore volume (cm ³ /g)	<i>d</i> (nm)
TiO ₂ -graphene composite nanofibers (9.9 wt % graphene)	191 ± 5	8.6	0.4	150 ± 50
bare TiO ₂ nanofibers	52 ± 4	18.2	0.239	100 ± 63

initial discharge capacity of 260 mA h g⁻¹ at constant current density of 33 mA g⁻¹, and it corresponds to the insertion of 0.78 mol of Li per formula unit. In the first charge, the cell delivered a reversible capacity of 185 mA h g⁻¹ (0.55 mol of Li) against the theoretical capacity of 335 mA h g⁻¹ for 1 mol of lithium. In the present case, the reversible capacity, 185 mA h g⁻¹, is assumed to be 1 C and hence the applied current density 33 mA g⁻¹ belongs to 0.18 C. The irreversible capacity in the first cycle is estimated to be ~75 mA h g⁻¹, which corresponds to 0.22 mol of lithium. The cycling curves showed the shortened plateau regions or biphasic region at ~1.7 and ~2 V for discharge and charge, respectively. This shortened two-phase region correlates the information that interfacial lithium storage is slightly dominant rather than insertion.¹² The presence of a plateau region during the charge-discharge process reflects well with CV traces obtained above and confirmed that the Li insertion takes place by a two-phase reaction mechanism. Similar kind of shortened two-phase region was noted by other researchers for graphene-TiO₂ composites, for example, Ding et al.⁴⁰ for graphene/TiO₂ composites, Wang et al.⁴¹ for self-assembled TiO₂-graphene hybrid nanostructures, and Shen et al.⁴² for three-dimensional TiO₂-graphene-carbon nanotube nanocomposites. Figure 7b shows the cycling performance of Li/TiO₂-G cell cycled between 1 and 3 V at 33 mA g⁻¹. The cell showed an almost stable cycling profile; however, a meager amount of capacity fading is noted in the initial few cycles. Further, it is obvious to note that, after a few initial cycles, the Coulombic efficiency is

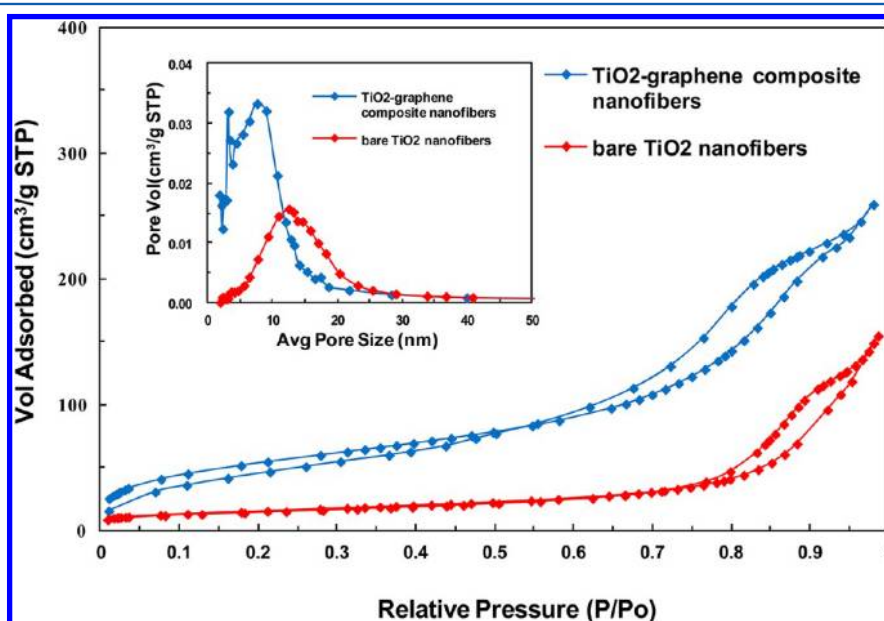


Figure 5. (a) N₂ adsorption and desorption isotherm of bare and TiO₂-graphene composite nanofibers and (b) pore size distribution.

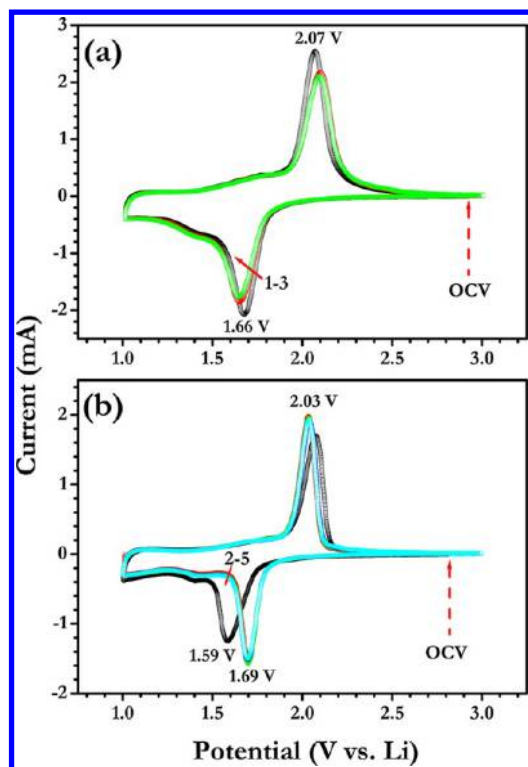


Figure 6. Cyclic voltammogram of (b) TiO_2 -graphene composite nanofibers and (a) TiO_2 bare nanofibers half-cells cycled between 1 and 3 V at a scan rate of 0.1 mV s^{-1} , in which metallic lithium serves as both counter and reference electrode.

found to be over 99%. The cell displayed the discharge capacity of 153 mA h g^{-1} after 100 cycles. The capacity fading was calculated after 10 initial cycles and is estimated to be ~ 0.23

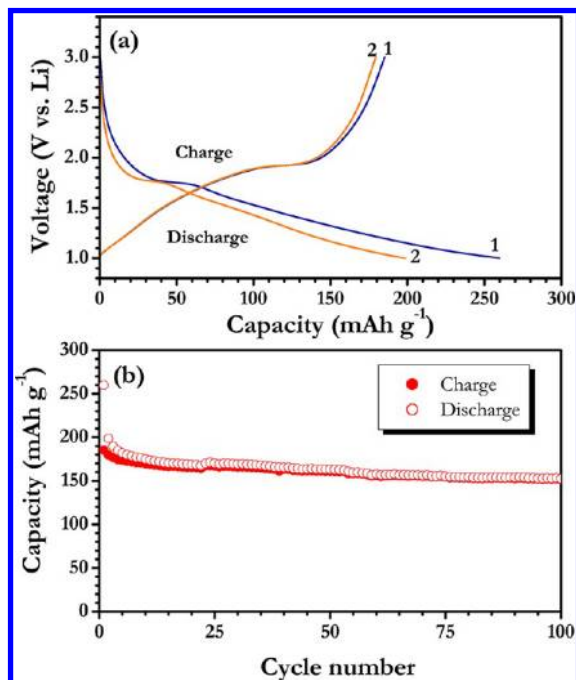


Figure 7. (a) Initial charge-discharge curves of Li/TiO_2 -graphene composite nanofibers half-cell cycled between 1 and 3 V at a current density of 33 mA g^{-1} at room temperature, and (b) cycling profiles of the Li/TiO_2 -graphene composite nanofiber cell.

mA h g^{-1} per cycle. The capacity fading in the initial cycles is due to the loss of symmetry during phase transition accompanied by a decrease in unit cell along the c -axis and a subsequent increase of unit cell volume ($\sim 4\%$) along the b direction that results in capacity fading.⁸ The obtained capacity is in good agreement with previous reports on TiO_2 -graphene composites.^{40–42}

The effect of graphene on the durability of anatase- TiO_2 nanofibers was evaluated for prolonged cycles in the same half-cell configurations at a relatively high current rate of 150 mA g^{-1} and compared with bare anatase TiO_2 nanofibers. The bare TiO_2 nanofibers were synthesized according to the synthesis procedure described in our previous work.³⁰ The cycling studies of bare and TiO_2 -G nanofibers are conducted for 300 cycles between 1 and 3 V at room temperature and illustrated in Figure 8. TiO_2 -G nanofibers exhibited an initial capacity of

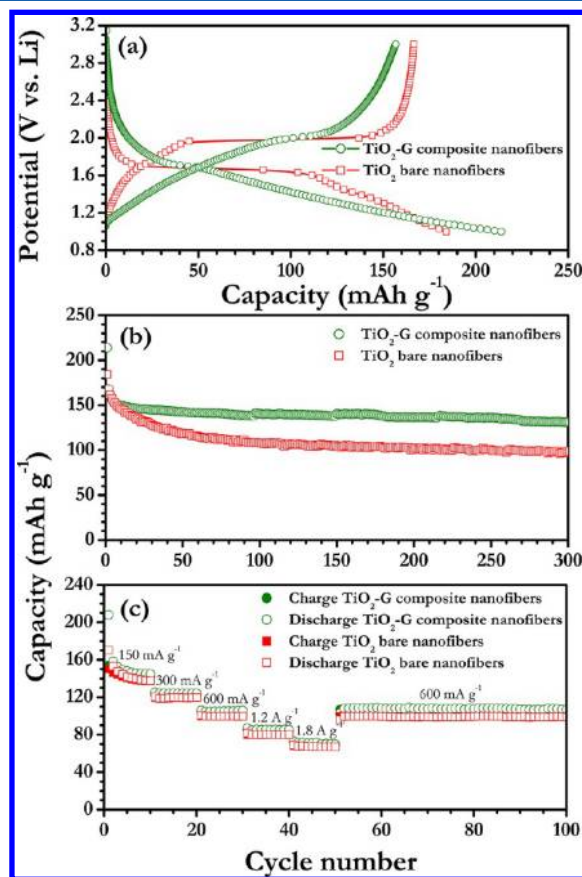


Figure 8. (a) Initial charge-discharge curves of bare TiO_2 nanofibers and TiO_2 -graphene composite nanofibers cycled between 1 and 3 V vs Li at a current density of 150 mA g^{-1} and (b) cycling profiles and (c) cells with different current densities.

214 mA h g^{-1} , which is higher than that of bare TiO_2 nanofibers (184 mA h g^{-1}). After 300 cycles, TiO_2 -G nanofibers and bare TiO_2 nanofibers gave discharge capacities of 131 and 98 mA h g^{-1} , respectively, at a current density of 150 mA g^{-1} . At the end of 300 cycles, TiO_2 -G nanofibers exhibited a higher reversible capacity retention of 84% as compared to 59% for bare TiO_2 . This improvement in the capacity retention of TiO_2 -G composites nanofibers is attributed to the presence of interconnecting, highly electronically conducting graphene amidst the titania nanofibers. The graphene nanosheets enable the faster transportation of

electrons at high current operations, which leads to enhanced cell performance. Furthermore, the 1D nanostructural fibers with highly exposed surface area toward electrolytes provide the facile insertion/extraction of Li ions during high rate operations due to the shortened diffusion pathways compared to particulates (see Figure S4, Supporting Information). In order to establish the influence of graphene on the capacity retention properties, higher current rates were applied on both bare TiO_2 and TiO_2 -G cells (Figure 8c). The TiO_2 -G nanofiber cell exhibited discharge capacities of 125, 105, 86, and 71 mA h g^{-1} for current density of 300, 600, 1200, and 1800 mA g^{-1} , respectively, whereas bare TiO_2 fibers showed discharge capacities of 119, 99, 79, and 67 mA h g^{-1} for the same current densities. As expected, increasing current density leads to a decrease in discharge capacity profile because less participation or surface of the active material involved in electrochemical reaction causes such fade.⁴³ The obtained results clearly showed the improved capacity retention properties of composite TiO_2 -G fibers as compared to bare TiO_2 fibers. The presence of graphene is beneficial for the high rate performance of the cell for prolonged cycling with minimal capacity fade. Further studies such as altering the graphene concentration to suppress the irreversible capacity of TiO_2 -G nanofibers in the first cycle and improve the reversible capacity during prolonged cycling are in progress.

In order to validate the influence of graphene on the electronic conductivity of TiO_2 nanofibers, an electrochemical impedance spectroscopy (EIS) was utilized and a typical Nyquist plot is given in Figure 9. The EIS spectra comprises a

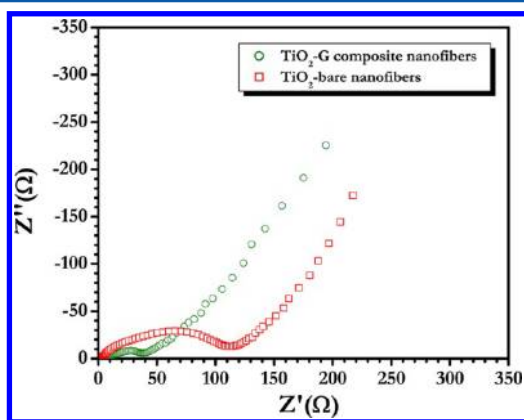


Figure 9. Electrochemical impedance spectroscopic traces of bare TiO_2 nanofibers and TiO_2 -graphene composite nanofibers.

semicircle followed by a vertically inclined tail; the appearance of such a high-frequency region is attributed to the formation of a solid electrolyte interface (SEI) film and/or contact resistance, and the medium frequency region is assigned to the charge-transfer (CT) impedance across the electrode/electrolyte interface.⁴⁴ The vertical tail inclined at 45° angle to the real axis corresponds to the lithium diffusion kinetics toward the electrodes called as Warburg tail.⁴⁵ From Figure 9, it can be observed that the diameter of the semicircle in the medium-frequency region for TiO_2 -G composite nanofibers is drastically suppressed as compared to bare TiO_2 nanofibers due to the introduction of highly conducting graphene in to the matrix. This reduction of medium frequency region is associated with the CT resistance and it is decreased from 112 to 36 Ω . The reduction of CT resistance is mainly

attributed to the improvement in the electronic conductivity profile offered by graphene nanosheets. This EIS study clearly authenticated that the incorporation of graphene sheets provides the improved conducting profiles for the TiO_2 -G composite nanofibers. The improvement in electronic conductivity profiles was well corroborated by electrochemical studies.

4. CONCLUSIONS

Anatase TiO_2 -graphene composite nanofibers (TiO_2 -G nanofibers) were synthesized for the first time using a simple electrospinning technique. Phase formation of anatase TiO_2 was confirmed by X-ray diffraction measurements and well supported by Raman and HR-TEM investigations. Fibrous morphology was clearly evident from the SEM and TEM pictures. The porous nature of electrospun TiO_2 -graphene composite nanofibers with high surface area was confirmed by BET and pore size analysis. Cyclic voltammetric analysis showed that the Li insertion/extraction takes place by a two-phase reaction mechanism and is reflected well in galvanostatic measurements. The durability of the TiO_2 -G fibers was evaluated in half-cell configuration and compared with bare anatase TiO_2 fibers for 300 cycles at 150 mA g^{-1} current density. The TiO_2 -G fibers retained 84% reversible capacity after 300 cycles, which is 25% higher than native TiO_2 fibers. This study clearly showed TiO_2 -G composite fibers are one of the prospective anode materials for high-power lithium ion batteries.

■ ASSOCIATED CONTENT

Supporting Information

TEM, SAED, and Raman spectra of graphene nanosheets are given along with TGA traces of polystyrene and the electrochemical profiles of graphene- TiO_2 nanoparticles are compared with present results and illustrated. This material is available free of charge via the Internet at <http://pubs.acs.org>.

■ AUTHOR INFORMATION

Corresponding Author

*E-mail: Madhavi@ntu.edu.sg (S.M.), seeram@nus.edu.sg (S.R.).

Author Contributions

#These authors contributed equally to this work.

Notes

The authors declare no competing financial interest.

■ ACKNOWLEDGMENTS

This work was supported by Singapore NRF-CRP grant on "Nanonets for Harnessing Solar Energy and Storage" and the FRC Startup grant R-265-000-361-133, National University of Singapore, Singapore. V.A. and S.M. wish to thank the National Research Foundation, Singapore, for the financial support through Clean Energy Research Project (NRF2009EWT-CERP001-036).

■ REFERENCES

- (1) Park, O. K.; Cho, Y.; Lee, S.; Yoo, H.-C.; Song, H.-K.; Cho, J. *Energy Environ. Sci.* **2011**, 4 (5), 1621–1633.
- (2) Song, M.-K.; Park, S.; Alamgir, F. M.; Cho, J.; Liu, M. *Mater. Sci. Eng., R* **2011**, 72 (11), 203–252.
- (3) Goodenough, J. B.; Kim, Y. *Chem. Mater.* **2009**, 22 (3), 587–603.

- (4) Etacheri, V.; Marom, R.; Elazari, R.; Salitra, G.; Aurbach, D. *Energy Environ. Sci.* **2011**, 4 (9), 3243–3262.
- (5) Aravindan, V.; Gnanaraj, J.; Madhavi, S.; Liu, H. K. *Chem.—Eur. J.* **2011**, 17 (51), 14326–14346.
- (6) Yang, Z.; Choi, D.; Kerisit, S.; Rosso, K. M.; Wang, D.; Zhang, J.; Graff, G.; Liu, J. *J. Power Sources* **2009**, 192 (2), 588–598.
- (7) Kavan, L. *Chem. Rec.* **2012**, 12 (1), 131–142.
- (8) Sudant, G.; Baudrin, E.; Larcher, D.; Tarascon, J. M. *J. Mater. Chem.* **2005**, 15 (12), 1263–1269.
- (9) Liu, J.; Xue, D. *Nanoscale Res. Lett.* **2010**, 5 (10), 1525–1534.
- (10) Reddy, M. V.; Jose, R.; Teng, T. H.; Chowdari, B. V. R.; Ramakrishna, S. *Electrochim. Acta* **2010**, 55 (9), 3109–3117.
- (11) Nam, S. H.; Shim, H.-S.; Kim, Y.-S.; Dar, M. A.; Kim, J. G.; Kim, W. B. *ACS Appl. Mater. Interfaces* **2010**, 2 (7), 2046–2052.
- (12) Shin, J.-Y.; Samuelis, D.; Maier, J. *Adv. Funct. Mater.* **2011**, 21 (18), 3464–3472.
- (13) Su, D. S.; Schlögl, R. *ChemSusChem* **2010**, 3 (2), 136–168.
- (14) Liu, X.-M.; Huang, Z. d.; Oh, S. w.; Zhang, B.; Ma, P.-C.; Yuen, M. M. F.; Kim, J.-K. *Compos. Sci. Technol.* **2012**, 72 (2), 121–144.
- (15) Zhu, Y.; Murali, S.; Cai, W.; Li, X.; Suk, J. W.; Potts, J. R.; Ruoff, R. S. *Adv. Mater.* **2010**, 22 (35), 3906–3924.
- (16) Sun, Z.; James, D. K.; Tour, J. M. *J. Phys. Chem. Lett.* **2011**, 2 (19), 2425–2432.
- (17) Pumera, M. *Chem. Rec.* **2009**, 9 (4), 211–223.
- (18) Zhu, X.; Zhu, Y.; Murali, S.; Stoller, M. D.; Ruoff, R. S. *ACS Nano* **2011**, 5 (4), 3333–3338.
- (19) Zhu, X.; Zhu, Y.; Murali, S.; Stoller, M. D.; Ruoff, R. S. *J. Power Sources* **2011**, 196 (15), 6473–6477.
- (20) Li, B.; Cao, H.; Shao, J.; Li, G.; Qu, M.; Yin, G. *Inorg. Chem.* **2011**, 50 (5), 1628–1632.
- (21) Shen, L.; Yuan, C.; Luo, H.; Zhang, X.; Yang, S.; Lu, X. *Nanoscale* **2011**, 3 (2), 572–574.
- (22) Su, J.; Cao, M.; Ren, L.; Hu, C. *J. Phys. Chem. C* **2011**, 115 (30), 14469–14477.
- (23) Zhou, G.; Wang, D.-W.; Li, F.; Zhang, L.; Li, N.; Wu, Z.-S.; Wen, L.; Lu, G. Q.; Cheng, H.-M. *Chem. Mater.* **2010**, 22 (18), 5306–5313.
- (24) Zhu, N.; Liu, W.; Xue, M.; Xie, Z.; Zhao, D.; Zhang, M.; Chen, J.; Cao, T. *Electrochim. Acta* **2010**, 55 (20), 5813–5818.
- (25) Tao, H.-C.; Fan, L.-Z.; Yan, X.; Qu, X. *Electrochim. Acta* **2012**, 69 (0), 328–333.
- (26) Dong, Z.; Kennedy, S. J.; Wu, Y. *J. Power Sources* **2011**, 196 (11), 4886–4904.
- (27) Cavaliere, S.; Subianto, S.; Savych, I.; Jones, D. J.; Roziere, J. *Energy Environ. Sci.* **2011**, 4 (12), 4761–4785.
- (28) Cheah, Y. L.; Gupta, N.; Pramana, S. S.; Aravindan, V.; Wee, G.; Srinivasan, M. *J. Power Sources* **2011**, 196 (15), 6465–6472.
- (29) Prasanth, R.; Aravindan, V.; Srinivasan, M. *J. Power Sources* **2012**, 202 (0), 299–307.
- (30) Kumar, P. S.; Nizar, S. A. S.; Sundaramurthy, J.; Ragupathy, P.; Thavasi, V.; Mhaisalkar, S. G.; Ramakrishna, S. *J. Mater. Chem.* **2011**, 21 (26), 9784–9790.
- (31) Sahay, R.; Sundaramurthy, J.; Suresh Kumar, P.; Thavasi, V.; Mhaisalkar, S. G.; Ramakrishna, S. *J. Solid State Chem.* **2012**, 186 (0), 261–267.
- (32) Bao, Q.; Zhang, H.; Yang, J.-x.; Wang, S.; Tang, D. Y.; Jose, R.; Ramakrishna, S.; Lim, C. T.; Loh, K. P. *Adv. Funct. Mater.* **2010**, 20 (5), 782–791.
- (33) Vorkapic, D.; Matsoukas, T. *J. Am. Ceram. Soc.* **1998**, 81 (11), 2815–2820.
- (34) Ferrari, A. C.; Robertson, J. *Phys. Rev. B* **2000**, 61 (20), 14095–14107.
- (35) Ohsaka, T.; Izumi, F.; Fujiki, Y. *J. Raman Spectrosc.* **1978**, 7 (6), 321–324.
- (36) Zhang, W. F.; He, Y. L.; Zhang, M. S.; Yin, Z.; Chen, Q. *J. Phys. D: Appl. Phys.* **2000**, 33 (8), 912.
- (37) Yoo, E.; Kim, J.; Hosono, E.; Zhou, H.-s.; Kudo, T.; Honma, I. *Nano Lett.* **2008**, 8 (8), 2277–2282.
- (38) Patoux, S.; Masquelier, C. *Chem. Mater.* **2002**, 14 (12), 5057–5068.
- (39) Wagemaker, M.; Kentjens, A. P. M.; Mulder, F. M. *Nature* **2002**, 418 (6896), 397–399.
- (40) Ding, Y.-H.; Zhang, P.; Ren, H.-M.; Zhuo, Q.; Yang, Z.-M.; Jiang, Y. *Mater. Res. Bull.* **2011**, 46 (12), 2403–2407.
- (41) Wang, D.; Choi, D.; Li, J.; Yang, Z.; Nie, Z.; Kou, R.; Hu, D.; Wang, C.; Saraf, L. V.; Zhang, J.; et al. *ACS Nano* **2009**, 3 (4), 907–914.
- (42) Shen, L.; Zhang, X.; Li, H.; Yuan, C.; Cao, G. *J. Phys. Chem. Lett.* **2011**, 2 (24), 3096–3101.
- (43) Zaghbi, K.; Goodenough, J. B.; Mauger, A.; Julien, C. *J. Power Sources* **2009**, 194 (2), 1021–1023.
- (44) Lin, Y.-M.; Abel, P. R.; Heller, A.; Mullins, C. B. *J. Phys. Chem. Lett.* **2011**, 2 (22), 2885–2891.
- (45) Yang, S.; Song, H.; Chen, X. *Electrochem. Commun.* **2006**, 8 (1), 137–142.